High-Performance Flexible PbS Nanofilm Wavelength Sensor with Detection Region Ranging from DUV to NIR

Feng-Xia Liang,[1,3] Yi Hu,[2] Zhi-Guo Zhu,[1] Zhi-Cheng Wu,[1] Jie Yu,[2] Li-Yan Liang,[1] Jiang Wang,[1] Li Wang,[1] Chun-Yan Wu,[1] Ping-An Song,[3] Lin-Bao Luo[1]**

[1] *School of Microelectronics, Hefei University of Technology, Hefei, Anhui 230009, China.*

[2] *School of Materials Science and Engineering, Hefei University of Technology, Hefei, Anhui 230009, China.*

[3] *Centre for Future Materials, University of Southern Queensland, Springfield 4300 Australia*

Corresponding authors: Pingan.Song@unisq.edu.au,luolb@hfut.edu.cn

Abstract

In this study, we report on the fabrication of a flexible wavelength sensor, which was achieved by growing a layer of lead sulfide (PbS) nanofilm on both sides of a PET substrate using chemical bath deposition method, followed by deposition of two parallel Au interdigital electrodes. Experimental result shows that the photocurrent ratio of the two photodetectors monotonically decreases with increasing wavelength in the range from 265 nm (UV) to 2000 nm (NIR), indicating that the incident light wavelength can be distinguished by the photocurrent ratio. Notably, the as-constructed wavelength sensor exhibits superior performance compared to most previously reported filter-less designs, achieving an average absolute error of 11.5 nm and an average relative error of 1.1%. It is also found that the sensor exhibits excellent mechanical flexibility and environmental stability. Furthermore, by introducing the back-end circuit, real-time detection of the wavelength of monochromatic light and the peak wavelength of LED light were achieved, with detection errors not exceeding 1.8% and 2.6%, respectively. It is believed that the flexible PbS nanofilm wavelength sensor prepared in this study has potential application in future portable and flexible optoelectronic devices.

Introduction

Wavelength (or color) sensors which are capable of distinguishing wavelengths within a specific range have garnered significant research interest in various fields, including visible light communications (VLC), artificial intelligence-assisted driving, image sensing, machine vision, and non-destructive testing of components.[1-5] The auxiliary structures like optical filters that are not part of the photoactive layer, are often employed to help filter the wavelength in these sensors.[6-8] To further facilitate the miniaturization of devices, specialized strategies to manipulate the materials within the photoactive layer have been developed to realize wavelength or color discrimination.[9-13] For example, Polzer *et al.* have proposed a filter-less RGB color sensor fabricated by the standard 0.6 μm Bipolar Complementary Metal-Oxide-Semiconductor (BiCMOS) technology for wavelength detection in the 400-900 nm range, which consists of three vertically stacking photodiodes with deep and shallow p-n junctions integrated on silicon.[9] However, the CMOS technology based on silicon usually involves complex fabrication processes employing expensive manufacturing equipment. Yang and his coworkers have demonstrated a nanowire spectrometer made from CdS_xSe_{1-x} nanowires with compositional gradients, and the resolution achieved by the nanowire spectrometer is around 10 nm for visible light spectrum reconstruction.[12] Benefiting from the simple solution process, some organic materials are also employed as photoactive layers.[4, 14, 15] What is more, Fukuda et al. has developed a trichromatic flexible sensor through the spin-coating process, capable of selectively absorbing blue, green, and red light.[16] Xiao's group integrated organic photodiodes (OPDs) onto high-resolution organic thin-film transistor (OTFT) backplanes on plastic substrate, creating a large-size, ultra-flexible organic image sensor array using solution coating processes at low temperatures.[17] In spite of these efforts, these inorganic or organic-based filter-less based devices still have their own shortcomings, such as reliance on relatively complex material synthesis routes or the instability of the materials. Moreover, it is noted that most of the reported filter-less work focuses on qualitative color recognition, while some of devices can recognize incident wavelength in a quantitative manner, with poor wavelength resolution which is far away from satisfactory.

Recently, our group has proposed a filter-less carrier-selective collection mechanism to construct a novel and simple structure, which has shown excellent performance.[18-20] For instance, by utilizing such mechanism, Si has been employed to quantitatively determine the wavelength in broad detection ranges from 265 to 1050 nm, with a good wavelength resolution of 1 nm.[20] Nevertheless, this device is characterized by using rigid substrate of Si, Ge, or glass,[18-21] which restrict their potential

application in the flexible electronics. In light of this, we herein put forward a flexible PET substrate and lead sulfide (PbS) nanofilms with relatively small bandgap, in an effort to expand its application field and wavelength detection ranges. The PbS nanofilms were grown on both sides of the PET by chemical bath deposition (CBD)[22, 23] and two parallel Au interdigital electrodes were deposited respectively on the as-synthesized nanofilm to assemble two vertically stacking photodetectors (PDs). Technical computer-aided design (TCAD) simulations demonstrate that the PbS nanofilms exhibit different photogeneration rates and penetration depths under radiation of varying wavelengths, leading to distinct spectral responses of the upper and lower PD in the as-constructed sensor. Further device analysis revealed that the corresponding photocurrent ratio decreases monotonically with increasing wavelength, making the recognition of wavelength possible in a broad detection range from 265 to 2000 nm, with the average absolute error and average relative error to be 11.5 nm and 1.1%, respectively. Furthermore, the as-constructed wavelength sensor possesses good mechanical flexibility and environmental stability. Under different bending angles and bending cycles, the photocurrent ratio does not show significant variation (less than 4.49%) and a monotonic relationship between the photocurrent ratio and wavelength is still well maintained. Finally, by integrating the as-constructed sensor into the back-end circuit, various monochromatic lights and the peak wavelengths of LED lights (450, 530, 660 nm) were recognized, with detection errors less than 1.8% and 2.6%, respectively. With the flexible structure, low-cost manufacturing process, and wide detection range, this sensor shows great promise for use in portable and flexible optoelectronic devices in the future.

Results and discussion

The proof-of-concept wavelength sensor which is composed of two identical PbS polycrystalline nanofilm based PDs (PD1 and PD2) is depicted in **Figure 1**a. The device actually relies on the simultaneous growth of PbS nanofilms with the same thickness on both sides of a PET substrate using a CBD method,[23] followed by the deposition of two parallel Au interdigital electrodes. Figure S1 (Supporting Information) provides details of the PbS growth and sensor fabrication process. Note that the PET substrate was positioned perpendicular to the bottom of the beaker, in order to ensure that the thickness of the PbS nanofilms grown on both sides of the substrate are the same. The SEM image on the right of Figure 1a clearly shows the surface morphology of the as-fabricated PD, with the interdigital electrodes' widths of 200 μm and a spacing of 190 μm on the PbS film. X-ray diffraction (XRD) pattern of the PbS nanofilms is shown in Figure 1b, and the peaks at 25.9°, 30.0°, 42.9°, and

50.9° correspond to (111), (200), (220), and (311) planes of PbS, respectively. These peaks are in agreement with the cubic phase of PbS ([PDF #05-0592]).[24] No additional spurious peaks are detected, indicating high purity of PbS film. Energy dispersive spectroscopy (EDS) analysis in Figure 1c shows a Pb/S elemental ratio of 49.6:50.4%, which is consistent with the stoichiometric ratio of PbS. Additionally, Pb and S atoms are uniformly distributed throughout the PbS nanofilm.

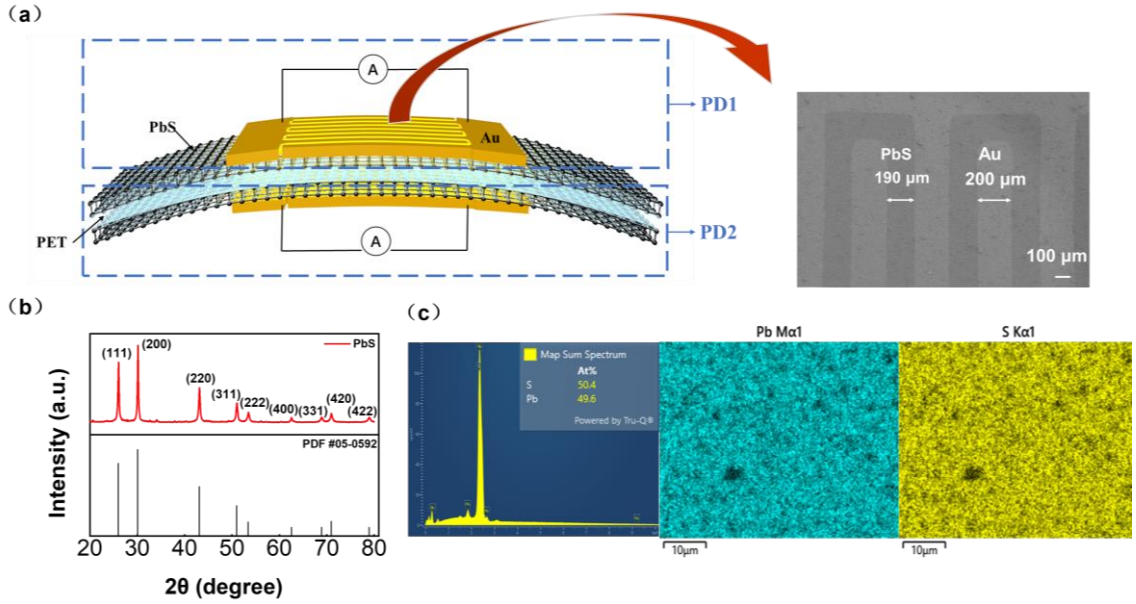

Figure 1. (a) Schematic illustration of the as-fabricated wavelength sensor and the SEM image of the PD. (b) The XRD pattern of the PbS film. (c) EDS result and elemental mapping of both Pb and S elements.

Even though the two photodetectors are similar in thickness, they however display different photon absorption in the depth direction of the film. The photogeneration rate (G) of a PbS film (thickness: 2000 nm) was simulated at different wavelengths (200 ~ 2000 nm) using the Silvaco TCAD technique. **Figure 2**a illustrates that the photogeneration rate, from which one can easily find that the photogeneration rate decrease from the top to the bottom of the film at any wavelength. As the simulated wavelength increases, the region with a relatively higher photogeneration rate extends and gradually shifts from the surface to the entire depth. These simulation results is reasonable due to the fact that the absorption coefficient decreases dramatically with increasing wavelengths, as depicted in Figure 2b. Noted that the absorption coefficient (α) of PbS is calculated using the extracted data of λ and k in the following formula (1):[25]

$$\alpha = \frac{4\pi k}{\lambda} \quad (1)$$

Where λ is the wavelength of incident light, and k is the extinction coefficient of PbS. To further

visualize the effect of thickness, the light absorption of PbS nanofilms with different thicknesses (20 to 3000 nm) were simulated using finite-difference time-domain (FDTD), as shown in Figure 2c. Considering the relatively low band gap of PbS (0.41 eV), the absorption was simulated in the ultraviolet-visible-near-infrared (UV-VIS-NIR) bands of 200-2000 nm. From the figure, it is evident that as the thickness increases, the total light absorption intensity of the PbS nanofilm increases, which is understandable as more photons are absorbed in a thicker film. Further careful observation finds that as the thickness decreases, the proportion of long-wavelength light (visible and near-infrared) absorption intensity gradually decreases, and the peak of light absorption shows a significant blue shift, which is consistent with the photogeneration rate distribution.[23] Based on the simulation results described above, the distribution of electron-hole pairs in the designed sensor under illumination of short, medium, and long wavelengths of light is shown in Figure 2d. It is noteworthy that the upper part of PD1, is more likely to collect electrons generated by short-wavelength light compared to the relatively longer-wavelength light detected by PD2.

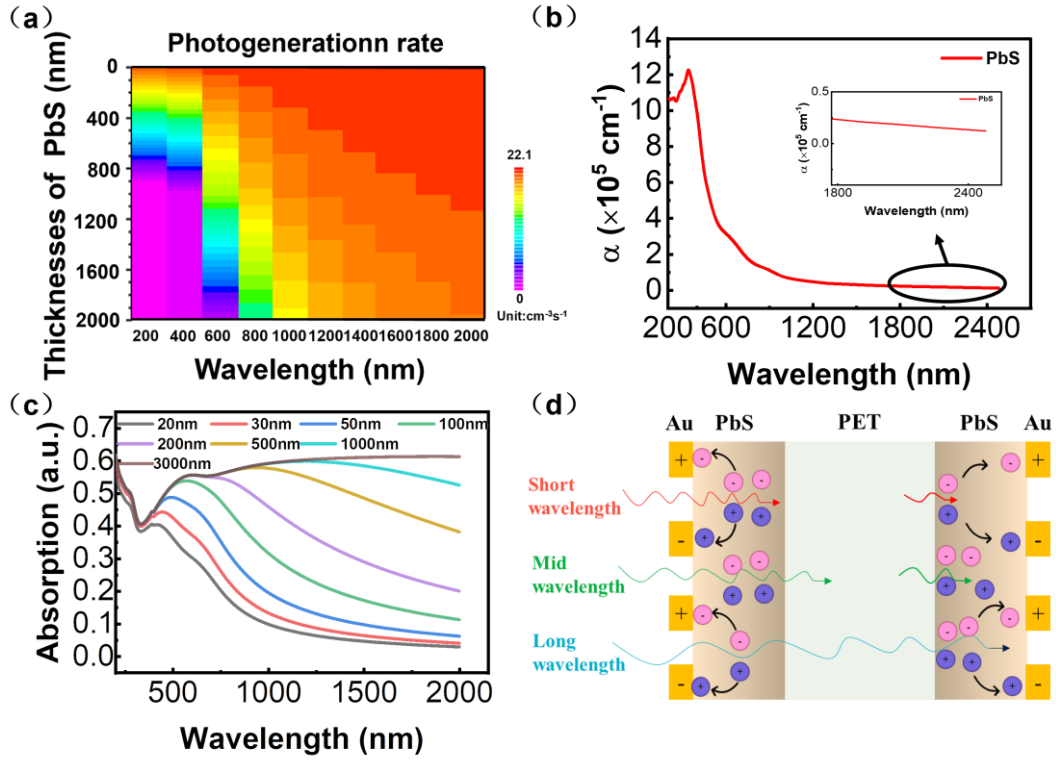

Figure 2. (a) Simulated photogeneration rate under different wavelengths of illumination. (b) The absorption coefficient of PbS as a function of wavelength. (c) The absorption spectra of PbS films with thicknesses of 20 nm, 30 nm, 50 nm, 100 nm, 200 nm, 500 nm, 1000 nm, 3000 nm at 200-2000 nm. (d) Schematic of the wavelength sensor.

Next, a series of wavelength sensors with varying thicknesses of PbS films were fabricated in the experiments through immersing the PET substrate into the PbS precursor solution for different durations. The obtained PbS nanofilms with different thicknesses were characterized by Atomic Force Microscopy (AFM), as shown in Figure S2 (Supporting Information). According to the height profiles of the PbS nanofilms, the thicknesses of 207 nm, 414 nm, and 878 nm are achieved. Subsequently, the optoelectronic properties of the corresponding wavelength sensors with different PbS thicknesses were measured and analyzed. **Figure 3**a presents the photocurrent curves of PD1 (I_1) and PD2 (I_2), under a bias voltage of 1 V and an incident light intensity of 200 μW/cm^2. It is found that the two PDs in each wavelength sensor exhibit quite different spectral response characteristics under vertically incident light irradiation. Taking the wavelength sensor with a thickness of 414/414 nm for example, PD1 shows the maximum response at 1400 nm and a photocurrent magnitude of 22.60 μA, whereas the PD2 exhibits a maximum response at 1450 nm with a photocurrent of 5.20 μA. Clearly, compared with the upper PD1, the PD2 absorbs less light, and the peak of its spectral response shifts to a relatively longer wavelength, which is consistent with the variation tendency of the simulated photogeneration rate distribution and absorption. Finally, the corresponding photocurrent ratio (I_1/I_2) was calculated for each film thickness in Figure 3b. Interestingly, the I_1/I_2 as a function of wavelength shows a monotonic trend for the wavelength sensor with a thickness of 414/414 nm PbS film over the broad wavelength range from 265 nm to 2000 nm. Such monotonic relationship is similar to what has been observed in Si, Ge and perovskite based wavelength sensors with similar device geometries.[18-20, 26] In comparison with the 414/414 nm PbS film, the 817/817 nm PbS film-based wavelength sensor also exhibits a good monotonic characteristic, with a detection range from 300 to 2000 nm wavelength. The decrease in detection range could be explained by the limited amount of light reaching PD2 for wavelengths below 300 nm, which is caused by the shadow effect of the thicker upper layer PD1. However, for the 207/207 nm wavelength sensor, non-monotonic behavior in the range of 980-2000 nm is displayed in the inset of Figure 3b. This may be due to the approximate absorption of PD1 and PD2 at such wavelength ranges. Therefore, a 414/414 nm PbS film-based device is employed in the following investigations.

Further experimental results indicate that the relationship between wavelength and photocurrent ratio is also influenced by the light intensity and bias voltage. The spectral response of the stacked PDs in the sensor was measured at light intensities of 200, 400, and 800 μW/cm^2, as shown in Figure S3a (Supporting Information). It is evident that as the light intensity increases, both I_1 and I_2 increase

because stronger light generates more electron-hole pairs, leading to higher photocurrent in the device. Moreover, the numerical relationship, i.e., monotonic characteristic, between the photocurrent ratio (I_1/I_2) and the wavelength of incident light is still well maintained at all light intensities, although the photocurrent ratio is relatively higher at lower light intensities (Figure 3c). This phenomenon could be attributed to the fact that the photocurrent of two devices (PD1 and PD2) can be affected to different extents by the light intensity, which results in a higher photocurrent ratio at low intensity compared to that at high intensity. Additionally, the effect of bias voltage on the sensor was investigated. As illustrated in Figure S3b (Supporting Information), the increase in bias voltage can enhance the photocurrent due to the larger electric field's facilitative effect on the effective separation of carriers and its inhibitory effect on carrier recombination. Figure 3d depicts the wavelength-dependent photocurrent ratio I_1/I_2 at different voltages, which shows similar monotonic trend. These results indicate that the wavelength sensor can detect wavelengths at different light intensities and bias voltages.

Although the achieved monotonic curve between photocurrent ratio and wavelength is not linear, it can be described segmentally using the Allometric fitting (265-1010 nm) and Boltzmann fitting (1010-2000 nm) (Figure 3e), and the following equation (2) could be derived correspondingly:

$$\lambda = \begin{cases} exp\left(-\frac{1}{2.578} ln \frac{\frac{I_1}{I_2}}{9.487\times10^8}\right), \ 265\ nm \leqslant \lambda < 1010\ nm \\ 476.205\ ln\left(\frac{4151.881}{\frac{I_1}{I_2}+0.689} - 1\right) - 1811.05, \ 1010\ nm \leqslant \lambda \leqslant 2000\ nm \end{cases} \quad (2)$$

Where λ and I_1/I_2 are the wavelength and photocurrent ratio, respectively. To assess the accuracy of the fitted curves in quantifying the wavelengths, the absolute and relative errors were analyzed using the equation (3) and (4):

$$Absolute\ error = |\lambda_e - \lambda_t| \quad (3)$$

$$Relative\ error = \frac{|\lambda_e - \lambda_t|}{\lambda_e} \times 100\% \quad (4)$$

Where λ_t and λ_e denote the theoretical and experimental wavelengths, respectively. The corresponding calculated data using the above equations is shown in Table S1 (Supporting Information). Figure S4a and S4b (Supporting Information) summarize the absolute and relative errors for wavelengths from 265 to 2000 nm. The average absolute error over the entire sensing range was calculated to be 11.5 nm, with an average relative error of 1.1%. Also, it is worth noting that the device exhibits excellent environmental stability, as shown in Figure 3f. Even after 30 days of storage

in unprotected environmental condition, the photocurrent of the device did not show any obvious decrease (about 0.28%), which is attributed to the good stability of the PbS nanofilm. **Table 1** compares the achieved key parameters of our device and other main filter-assisted and filter-less wavelength sensors. It could be observed that the as-fabricated sensor presents comparable or superior resolution to a single CdS_xSe_{1-x} nanowire spectrometer (10 nm),[12] two stacked MLG/Ge heterojunction based wavelength sensor (6.1 nm, 0.5%)[19], a miniaturized spectrometer based on filter array integrated into a CMOS imager (40 nm, 8.5%) and a spectrometer with $KMAPbCl_xBr_{3-x}$ PDs array (80 nm).[6, 28] Additionally, although its average absolute error is inferior to that of a colloidal quantum dot spectrometer (2.5 nm), a sensor utilizing a triple p-n junction buried within BiCMOS technology (5 nm, 2.5%),[9, 27] the corresponding relative error of present device is very competitive. Therefore, it can be concluded that our as-fabricated PbS wavelength sensor exhibits comparable or better resolution to most of the lately reported wavelength sensor, but with a much broader detection range from UV to NIR.

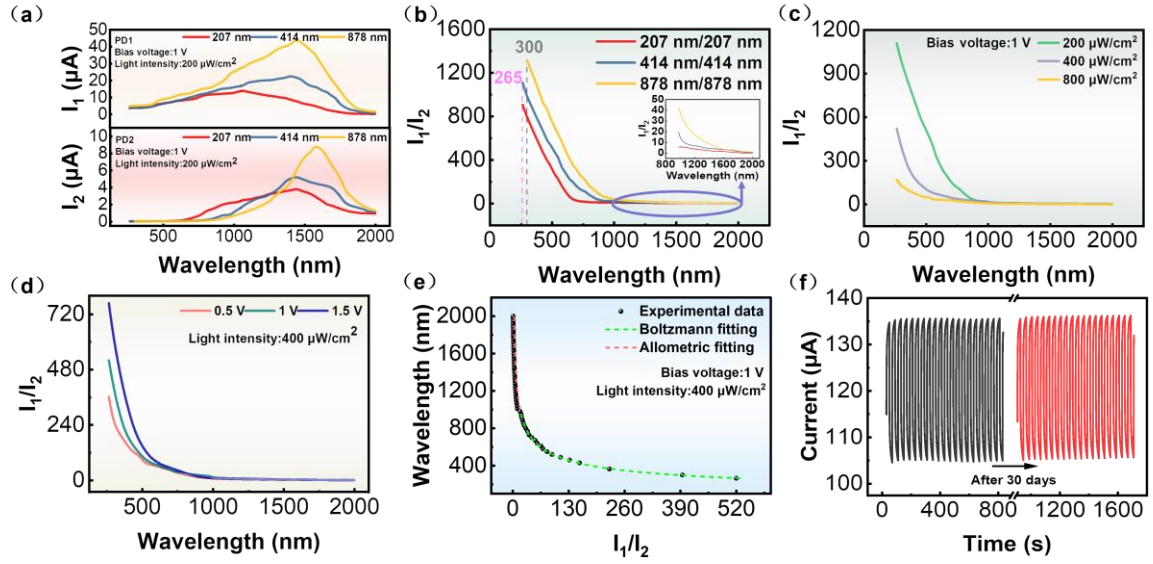

Figure 3. (a) Spectral response of PD1 and the PD2 of the wavelength sensor with PbS films of different thicknesses in the whole detection range, the light intensity is 200 μW/cm^2 and the bias voltage is 1 V. (b) Photocurrent ratio of the PD1 to the PD2 under PbS films of different thickness. Inset: Partial enlarged view. (c) Photocurrent ratios as a function of light intensity. (d) Photocurrent ratios as a function of bias voltage. (e) Subsection fitting curves: the green curve is Boltzmann fitting and red curve is Allometric fitting. (f) Comparison of time-dependent photoresponse for about 20 cycles before and after 30 days' air storage.

Table 1. Comparison of our device with the main filter assisted and filter-less wavelength sensors

Device structure	Detection range	Absolute error (nm)	Relative error (%)	Ref.
Two back-to-back PbS PDs on PET	265-2000	11.5	1.1	**This work**
CdS and CdSe colloidal quantum dots	390-690	2.5		[27]
Filter arrays integrated onto a CMOS imager	350-1050	40	8.5	[6]
Single CdS_xSe_{1-x} nanowire	380-700	10		[12]
$KMAPbCl_xBr_{3-x}$ PDs array	450-780	80		[28]
BiCMOS buried triple p-n junction	400-900	5	2.5	[9]
Two stacked MLG/Ge heterojunctions	880-1650	6.1	0.5	[19]

The reliability of the as-constructed wavelength sensor was further assessed by repeatedly bending the flexible PET substrate. **Figure 4**a shows the photocurrent variation of PD1, PD2, and the corresponding photocurrent ratios after bending the sensor for 500 cycles. The photocurrent of PD1 and PD2 exhibit maximum changes of 4.49% and 3.47%, and minimum changes of 0.09% and 0.49%, respectively. Correspondingly, the photocurrent ratio displays a maximum change of 2.47% and a minimum change of 0.60%, demonstrating the good bending stability of the constructed sensor. Furthermore, the mechanical flexibility was studied by bending the substrate to different angles. As illustrated in Figure 4b, the flexible PDs show negligible changes of photocurrent ratio and still maintain a well-defined monotonic relationship between the photocurrent ratio and wavelength, after bending from a planar state to 80° and 160° (the photograph in Figure 4c).

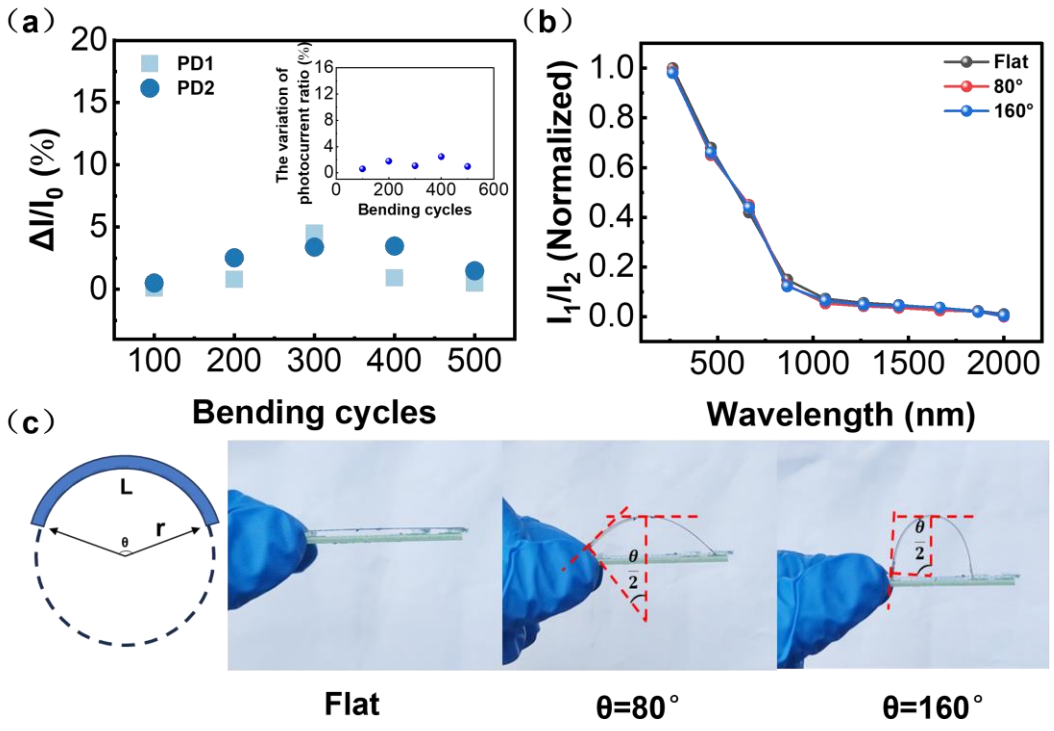

Figure 4. (a) The rate of photocurrent changes of the device after bending for 100, 200, 300, 400, and 500 cycles under 1450 nm illumination with a light intensity of 1 mW/cm^2 at a bias voltage of 1 V. Inset: The rate of photocurrent ratio change. (b) Normalized photocurrent ratio of devices with different bending degrees. (c) Schematic of the bending process.

Finally, by introducing backend circuits, the ability to visualize the wavelengths of monochromatic light and further detect the peak wavelengths of LED light were realized, which is crucial for production quantity management.[29-31] It should be noted that the light emitted by LEDs is typically polychromatic. However, the unique relationship between wavelength and photocurrent ratio is still applicable as long as the incident polychromatic light spectrum possesses a dominant wavelength and the spectrum's full width at half maximum is relatively narrow.[32, 33] In other words, this polychromatic light can be approximately considered as monochromatic light, and therefore, the photocurrent ratio can also be used to determine the peak wavelength of the LED light. To realize the detection of the wavelength, the electric current signals generated by the constructed PbS nanofilm sensor were converted into wavelength information related to the photocurrent ratio. **Figure 5**a illustrates the main components of the entire wavelength detection system. Due to the weak electric current signals, the microcontroller unit (MCU) is unable to collect and process them.[34, 35] Thus, two trans-impedance amplification circuits (U1, U2 and U4, U5) were used to amplify the current signals

from PD1 and PD2 into voltage signals, respectively. U3, a 4-channel analog switch, was used to adaptively select the appropriate range based on changes in the amplified voltage values. The analog-to-digital converter (ADC) then converted the continuous voltage signals into digital signals, which were processed by the MCU and displayed on the screen as voltage and specific wavelengths. According to the circuit in Figure S5 (Supporting Information), the power module, amplification circuit module, MCU module, detector module, and other modules were integrated on the printed circuit board, with the display screen connected to the circuit board by a serial cable, as shown in Figure S6 (Supporting Information).

To convert the photocurrent into wavelength, a relationship between the photocurrent ratio and wavelength should be established. Figure 5b shows the curves between the photocurrent ratio and wavelength under a light intensity of 1 mW/cm². Since LED light mostly fall within the visible spectrum, a wavelength range of 365-800 nm is chosen here for fitting with the Boltzmann function. This allows the establishment of the relationship between the photocurrent ratio (I_1/I_2) and wavelength (λ) as follows:

$$\frac{I_1}{I_2} = \frac{147.934}{1+exp\left(\frac{\lambda-326.604}{71.215}\right)} + 1.389 \quad (5)$$

After passing through a two-stage trans-impedance amplification circuit, the relationship between voltage (U) and the input current (I) is determined:

$$U_1 = R_1 I_1,\ R_1 = 1\ K\Omega \quad (6)$$

$$U_2 = R_2 I_2,\ R_2 = 1\ K\Omega \quad (7)$$

Finally, the relationship between λ and U_1/U_2 is derived from equation (4), (5), and (6):

$$\lambda = 71.215\ ln\left(\frac{147.934}{\frac{U_1}{U_2}-1.389} - 1\right) + 326.604 \quad (8)$$

It should be noted that when the light intensity changes, the relationship between I_1/I_2-λ and the corresponding λ-U_1/U_2 should be recalculated. This is because both the light intensity and wavelength simultaneously determine the photocurrent of the device. To demonstrate the practicality and reliability of the designed wavelength detection system, three monochromatic lights (450 nm, 530 nm, and 660 nm) were first tested, and the wavelengths were successfully displayed on the screen (Figure 5c). The detection errors for 450 nm, 530 nm, and 660 nm were 1.5%, 1.8%, and 1.6%, respectively. Considering the electromagnetic interference in the test space, as well as the influence of the wavelength sensor and amplifier circuits, and the fact that the chip was not protected with a metal shield, all of which can lead to various noise signals, such errors are acceptable. Further

demonstrations were performed using three LEDs with narrow half-maximum width spectra. Figures 5d-f present the spectral curves of LED lights with dominant wavelengths of 450, 530, 660 nm, as well as the values detected by the wavelength detection system. The detection errors for 450, 530, 660 nm LED lights were 2.1%, 2.6%, and 2.4%, respectively. In Figure 5g, the display shows the actual detected information (a detailed demonstration is shown in Supporting Information Video 1). These findings demonstrate the great potential of the constructed wavelength detection system in resolving different LED lights and its future application in industrial production and agricultural lighting.[33]

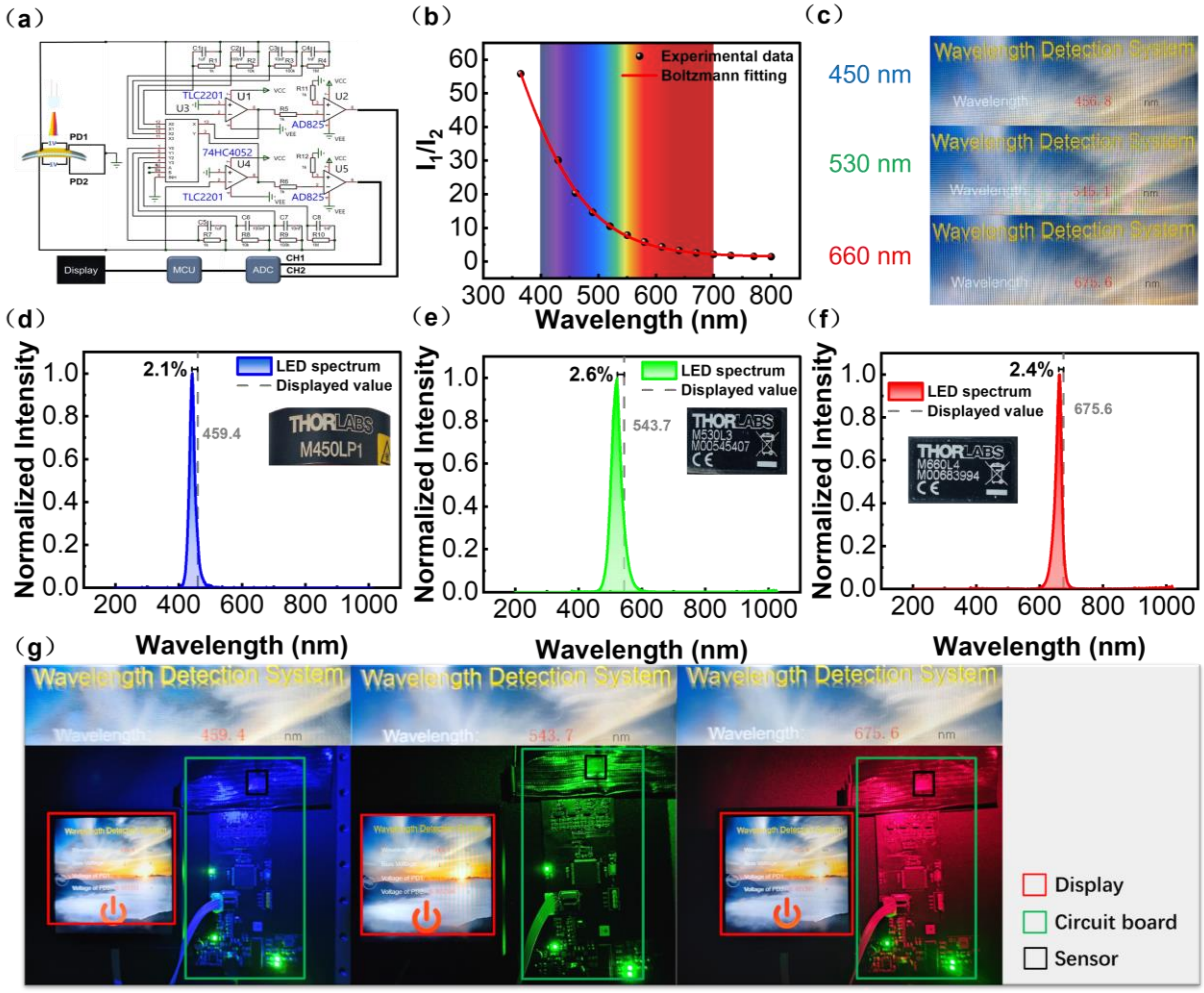

Figure 5. (a) Schematic diagram of wavelength detection system. (b) Wavelength detection system operating curve and test data. (c) The wavelength of monochromatic light and the results of detection. The spectra and detection results of LEDs with peak wavelengths of (d) 450nm, (e) 530nm, and (f) 660 nm. Inset: Information on the peak wavelength of LEDs. (g) The measured values of LEDs with three different peak wavelengths are displayed on the screen.

Conclusions

In summary, we have successfully fabricated a structurally simple wavelength sensor consisting of two back-to-back Au/PbS/Au PDs on a PET substrate. TCAD simulation results demonstrate that the sensor operates based on a wavelength-dependent photogeneration rate in the PbS film. The developed sensor could quantitatively resolve incident light wavelengths from 265 nm (UV) to 2000 nm (NIR), with an average relative error of 1.1%. Furthermore, the good flexibility and stability of the sensor have been demonstrated. At last, its capability to display the wavelength of the monochromatic lights and LEDs is shown through a home-made wavelength detection system with detection errors of no more than 1.8% and 2.6%, respectively. We believe this flexible wavelength sensor will play a significant role in the development of different optoelectronic devices.

Experimental Section

Material synthesis and device fabrication: First, the PET substrates were cleaned using an ultrasonic bath method with anhydrous ethanol and deionized water sequentially. After drying for 10 minutes, the PET was hydrophilized through oxygen plasma treatment. Then, the precursor solution of PbS was prepared by adding 20 ml of 1 mol/L sodium hydroxide (NaOH) to 5 ml of 1 mol/L lead nitrate [(Pb $(NO_3)_2$], stirring until fully dissolved. Next, 6 ml of 1 mol/L thiourea [$(H_2N)_2CS$], 4 ml of 1 mol/L triethanolamine [$(HOCH_2CH_2)_3$ N, TEA], and 65 ml of deionized water were added in sequence into the above solution. The as-obtained PbS precursor solution was preheated at 55 °C for 1 min, stirring while heating until completely dissolved (a small amount of black precipitate appeared in the solution). Once the above treatment was completed, the PET was placed vertically into the glass beaker to grow the PbS nanofilm. Noted that the PbS nanofilms with thicknesses of ~207, ~414 and ~878 nm was achieved through immersing the PET substrates into the precursor solution for ~24, ~48 and ~96 h, respectively. Finally, the as-obtained PbS nanofilms were cleaned by an ultrasonic cleaner to remove surface contaminants and loosely attached PbS particles. To fabricate the wavelength sensors, PET substrates with PbS nanofilms were divided into small pieces of the same size and transferred to the vacuum chamber of the electron beam evaporation coating machine. By using a metal shadow mask fabricated in the laboratory, 50 nm thick gold interdigital electrodes, with a width of 200 μm and a spacing of 190 μm, were deposited on PbS nanofilm layers on both sides of the PET.

Material characterization and device analysis: The thickness and structure of the PbS nanofilms

were characterized by atomic force microscopy (AFM, Dimension Icon) and X-ray diffraction (XRD, Rigaku D/max-rB). The morphology and elemental distribution of the films were characterized by SEM and EDS (Hitachi-SU8020). A supercontinuum fiber laser (SC-OM) was used as the illumination source and its light intensity was calibrated with a power meter (Thorlabs GmbH, PM 100D). The spectral response was obtained by testing the optoelectronic properties of the PDs by a semiconductor characterization system (Keithley 2400). All PDs were measured at room temperature.

Theoretical simulations: The Silvaco technology computer-aided design (TCAD) software was selected to simulate the photogeneration rate of PbS nanofilms. The structure of the device was first established in the two-dimensional simulation module of the ATLAS device simulation module, and then the material parameters and physical model were set. By defining the incident angle and light intensity, the simulated photogeneration rate of the device is finally obtained. Depending on the simulation results, the Tonyplot module can be used to output photogeneration rate spectra in different colors. The finite-difference time-domain (FDTD) method was selected to simulate the optical absorption of PbS nanofilms with different thicknesses at various wavelengths. The incident light was illuminated from the top with an incident angle of 90°. Perfectly matched layer (PML) boundary conditions were applied in the vertical direction.

Development of wavelength detection systems: To develop a wavelength detection system, the as-fabricated wavelength sensor, amplification circuit, and MCU are integrated on a PCB, and the detection results are displayed on a screen. The amplification circuit is designed using Altium Designer 20, and the MCU microcontroller program is written using C language. The LEDs used in the test were purchased from Thorlabs. To avoid interference in the detection results from captured reflected light, the area around the wavelength sensor is covered with black tape, leaving only the light-receiving part exposed. During wavelength detection, LEDs with wavelengths of 450, 530, and 660 nm are shone on the wavelength sensor, and the corresponding voltages and wavelengths are recorded on the display screen.

Supporting Information

The Supporting Information is available from the Wiley Online Library or from the author.

Acknowledgements

This work was supported by the National Natural Science Foundation of China (NSFC, No. 62074048, 61675062 and 62311530047), the Key Research and Development Plan of Anhui Province (2022f04020007), and the Fundamental Research Funds for the Central Universities (PA2020GDKC0014).

Conflict of Interest

The authors declare no conflict of interest.

Author Contributions

Y.H., Z.C.W. and J.Y. synthesized the samples and prepared the device, and analyzed the device performance. L.B.L. conceived the idea, supervised the whole project, and provided funding. Y.H. and L.Y.L simulated device. F.X.L. and P.A.S. contributed to the study of optical properties and physical mechanisms of materials. Z.G.Z. helped with simulation and testing of back-end circuits. J.W., L.W. and C.Y.W. compiled and analyzed the data.The manuscript is written by Y.H. and F.X.L. and discussed by all authors.

Data Availability Statement

The data that support the findings of this study are available from the cor-responding author upon reasonable request.

Keywords

wavelength sensor; PbS nanofilms; photodetector; flexible devices; the photocurrent rate.

References

[1] J. Cong, D. Yan, J. Tang, W. Guo, X. Mao, *IEEE Photonics Technology Letters* **2019**, *31*, 1979.
[2] D. Fernández Llorca, I. García Daza, N. Hernández Parra, I. Parra Alonso, *Sensors* **2020**, *20*, 5115.
[3] S. Hong, N. Zagni, S. Choo, N. Liu, S. Baek, A. Bala, H. Yoo, B. H. Kang, H. J. Kim, H. J. Yun, M. A. Alam, S. Kim, *Nature Communications* **2021**, *12*, 11.
[4] R. D. Jansen-van Vuuren, A. Armin, A. K. Pandey, P. L. Burn, P. Meredith, *Advanced Materials* **2016**, *28*, 4766.
[5] P. Muenstermann, R. Godding, M. Hermstein, *Proc. SPIE (USA)* **2017**, *10117*, 1011708 (9 pp.).
[6] U. Kurokawa, B. I. Choi, C. C. Chang, *Ieee Sensors Journal* **2011**, *11*, 1556.
[7] K. Kumar, H. Duan, R. S. Hegde, S. C. Koh, J. N. Wei, J. K. Yang, *Nature nanotechnology* **2012**, *7*, 557.
[8] J. Wang, Y. Xing, F. Wan, C. Fu, C.-H. Xu, F.-X. Liang, L.-B. Luo, *Journal of materials chemistry C* **2022**, *10*, 12929.
[9] A. Polzer, W. Gaberl, H. Zimmermann, *Electronics Letters* **2011**, *47*, 614.
[10] N. Ganesh, R. Shivanna, R. H. Friend, K. Narayan, *Nano Letters* **2019**, *19*, 6577.
[11] M. I. Hossain, H. A. Khan, M. Kozawa, W. Qarony, A. Salleo, J. Y. Hardeberg, H. Fujiwara, Y. H. Tsang, D. Knipp, *ACS applied materials & interfaces* **2020**, *12*, 47831.

[12] Z. Y. Yang, T. Albrow-Owen, H. X. Cui, J. Alexander-Webber, F. X. Gu, X. M. Wang, T. C. Wu, M. H. Zhuge, C. Williams, P. Wang, A. V. Zayats, W. W. Cai, L. Dais, S. Hofmann, M. Overend, L. M. Tong, Q. Yang, Z. P. Sun, T. Hasan, *Science* **2019**, *365*, 1017.
[13] S. Feruglio, G.-N. Lu, P. Garda, G. Vasilescu, *Sensors* **2008**, *8*, 6566.
[14] W. Wu, X. Wang, X. Han, Z. Yang, G. Gao, Y. Zhang, J. Hu, Y. Tan, A. Pan, C. Pan, *Advanced Materials* **2018**, *31*, 1805913.
[15] X. Zhang, X. Liu, Y. Huang, B. Sun, Z. Liu, G. Liao, T. Shi, *Frontiers of Mechanical Engineering* **2023**, *18*, 33.
[16] T. Fukuda, M. Komoriya, R. Kobayashi, Y. Ishimaru, N. Kamata, *Japanese Journal of Applied Physics* **2009**, *48*, 04C162.
[17] H. Xiao, T. Wei, C. Sujie, L. Jianghu, X. Hanyang, O. Bang, L. Ming, S. Yawen, C. Chun-Chao, P. Too, W. Xiaoqing, J. Libo, Q. Gang, G. Xiaojun, *2021 5th IEEE Electron Devices Technology & Manufacturing Conference (EDTM)* **2021**, DOI: 10.1109/edtm50988.2021.94208933 pp.
[18] F. X. Liang, R. Y. Fan, J. Y. Li, C. Fu, J. J. Jiang, T. Fang, D. Wu, L. B. Luo, *Small* **2021**, *17*.
[19] Y.-Z. Zhao, C. Fu, F.-X. Liang, Y.-T. Xiao, J.-Y. Li, M.-M. Liu, D. Wu, L.-B. Luo, *Journal of Materials Chemistry C* **2022**, *10*, 8474.
[20] C. Fu, C. Lu, H.-Y. Cheng, X. Zhang, Z.-X. Zhang, Y.-T. Xiao, D.-H. Lin, J. Wang, J.-G. Hu, Z.-L. Wang, D. Wu, L.-B. Luo, *IEEE Transactions on Electron Devices* **2022**, *69*, 2457.
[21] W.-H. Yang, X.-Y. Jiang, Y.-T. Xiao, C. Fu, J.-K. Wan, X. Yin, X.-W. Tong, D. Wu, L.-M. Chen, L.-B. Luo, *Materials Horizons* **2021**, *8*, 1976.
[22] W. L. Jiang, H. Deng, Q. Feng, X. Y. Li, *Chalcogenide Letters* **2021**, *18*, 449.
[23] Y. Wang, D. H. Lin, S. H. Luo, X. Zhang, C. Fu, J. Wang, C. Y. Wu, D. Wu, Y. X. Zhou, L. B. Luo, *Acs Applied Nano Materials* **2022**, *5*, 8894.
[24] B. H. Xie, G. T. Fei, S. H. Xu, X. D. Gao, J. X. Zhang, L. De Zhang, *Journal of Materials Chemistry C* **2018**, *6*, 1767.
[25] M. Grundmann, M. Grundmann, *The physics of semiconductors: an introduction including nanophysics and applications* **2010**, 775.
[26] C. Fu, Z.-Y. Li, J. Wang, X. Zhang, F.-X. Liang, D.-H. Lin, X.-F. Shi, Q.-L. Fang, L.-B. Luo, *Nano Letters* **2023**, *23*, 533.
[27] J. Bao, M. G. Bawendi, *Nature* **2015**, *523*, 67.
[28] H. X. Sun, W. Tian, X. F. Wang, K. M. Deng, J. Xiong, L. Li, *Advanced Materials* **2020**, *32*.
[29] H. Hamamoto, H. Shimaji, T. Higashide, *Journal of Agricultural Meteorology* **2003**, *59*, 103.
[30] H. Hamamoto, K. Yamazaki, *HortScience horts* **2009**, *44*, 1494.
[31] M. M. Hasan, T. Bashir, R. Ghosh, S. K. Lee, H. Bae, *Molecules* **2017**, *22*, 1420.
[32] S. Schidl, A. Polzer, H. Zimmermann, *Electronics letters* **2012**, *48*, 1490.
[33] B. R. Chen, S. Wang, K. Du, *Sensors and Actuators a-Physical* **2003**, *109*, 72.
[34] S. Zeng, W. Xiao, X. Hu, G. Teng, H. Gao, *2020 IEEE 2nd International Conference on Civil Aviation Safety and Information Technology (ICCASIT)* **2020**, DOI: 10.1109/iccasit50869.2020.9368749484.
[35] L. Lamberti, M. Rusci, M. Fariselli, F. Paci, L. Benini, *2021 IEEE International Symposium on Circuits and Systems (ISCAS)* **2021**, DOI: 10.1109/iscas51556.2021.94017301.